Chapter 7

Growth of Self-Organized TiO_2 Nanodot Arrays

7.1 Introduction

Semiconductor nanodots have attracted great interest because of their unique physical properties and promising applications in optoelectronic and microelectronic devices. They exhibit a wide range of size-dependent properties, and variations in fundamental characteristics ranging from phase transitions to electrical conductivity can be fine-tuned by controlling the size of the nanodots. One of the most probable approaches for preparing nanodots for device applications is the self-organized Stranski-Kranstanov growth in strained heterostructures[Eaglesham 1990-1943]. However, the spatial arrangement and size distribution of nanodots are random for most self-organized processes. In order to integrate the nanodots into practical applications, it is necessary to well control the alignment and size of nanodots on the substrate. Many techniques[Jin 1999-2752; Kitajima 2002-497; Mei 2002-361; Masuda 2000-1031] have been attempted to control the spatial arrangement and size distribution of nanodots. Ordered arrays of nanodots has been constructed by using nanoporous anodic aluminum oxide (AAO) membranes as an evaporation mask by Masuda *et al.*[Masuda 2000-1031]. Nanoporous AAO, which consists of vertical pore channel arrays with a hexagonal packing structure[Jessensky 1998-1173], is an ideal template for fabricating ordered arrays of nanostructured materials.

In this study, nanoporous AAO films was used as the mask for local anodization of titanium nitride (TiN) films to fabricate ordered nanodot arrays of titanium oxide (TiO_2). TiO_2 is one of the most important transition metal oxides, which has been proposed for a wide range of uses including photocatalysts[Linsebigler 1995-735; Anpo 1987-4305], photo-electrochemical cells[Grätzel 2001-338], gas detectors[Manno 1997-54], antireflection coatings[Crotty 1987-3077], and high-κ dielectrics[Lee 1999-3143]. In recent years, nanometer-sized tubules[Du 2001-3702], wires[Lei 2001-1125], and particles[Hua 2002-830; Bullen 2002-739] of TiO_2 have been intensively studied because of the large surface area and quantum size effects, which result in novel chemical, optical and electrical properties. The majority of previous studies used sol-gel[Du 2001-3702] or hydrolysis process[Lei 2001-1125; Zhang 2001-2511] to prepare TiO_2 nanostructures. In order to well control the dimension and morphology of TiO_2 nanostructures, nanoporous AAO was widely utilized as a template to selectively grow TiO_2 within the nanopores. In this study, ordered nanodot arrays of TiO_2 are formed by electrochemical anodization of the Al/TiN bilayered films on the silicon and sapphire substrates. When anodization of the aluminum upper layer is complete, anodic oxidation of the underlying TiN layer is confined in the pore area of the initially formed AAO, resulting in TiO_2 nanodot arrays with a uniform size distribution in accordance with the hexagonal order and pore size of the AAO nanopores. Since the as-prepared TiO_2 nanodots are basically amorphous, the post-growth annealing effect on phase development of the nanodots is also discussed. Using this novel approach, it is expected that nanodot arrays of various oxide semiconductors, which have an anodization behavior similar to that of TiO_2, may be fabricated, such as ZnO, In_2O_3, Fe_2O_3, SnO_2, WO_3, etc.

7.2 Preparation and microstructure of TiO_2 nanodots

Figure 7-1 illustrates the technological process for the preparation of nanodot arrays of titanium oxides. A sputtered TiN film of about 30 nm in thickness was first

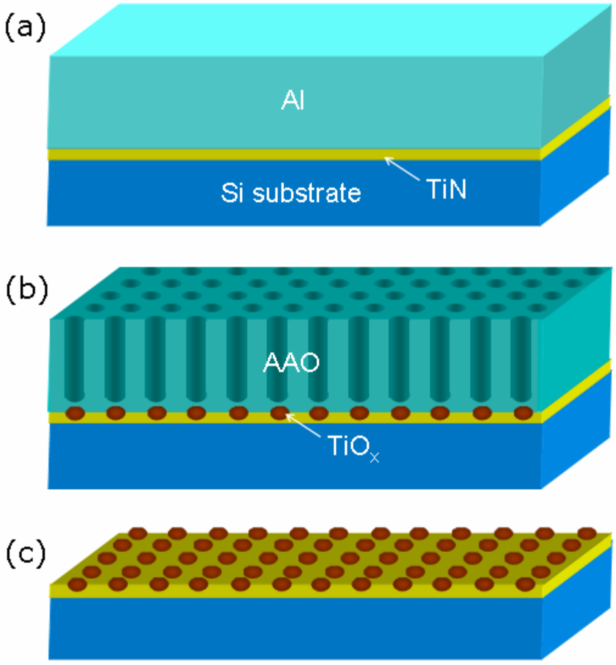

Figure 7-1 Schematic diagram showing the general steps of the formation process for titanium oxide nanodots under a porous AAO film: (a) Deposition of the Al/TiN bilayered films, (b) anodic oxidation for the nanoporous AAO and TiO_x nanodot formation, (c) selective removal of the overlying AAO film.

Table 7-1 Anodization conditions of the Al/TiN bilayered films for the preparation of titanium oxide nanodots.

Sample	**A**	**B**	**C**
Voltage	40 V	20 V	8 V
Electrolyte	$H_2C_2O_4$	H_2SO_4	H_2SO_4
Concentration	0.3 M	0.6 M	1.2 M
Bath temperature	21 °C	21 °C	21 °C

deposited on the *p*-silicon (100) wafer, followed by deposition of an aluminum film of 6 μm in thickness by thermal evaporation. The TiN film was deposited in an ultrahigh vacuum reactive dc magnetron sputtering system (MRC PRIMUS 2500TM), with a base pressure of 5×10^{-9} Torr. The aluminum film was deposited in a high vacuum chamber (< 5×10^{-7} Torr) using an aluminum source with a purity of 99.999%. Prior to anodization, the sample was annealed at 500 °C in a high vacuum furnace (about 1×10^{-7} Torr) for 8 hours to recrystallize the aluminum film, and then electropolished in a mixed solution of perchloric acid ($HClO_4$) and ethanol (C_2H_5OH) to obtain a smooth surface. Anodization was carried out in three types of aqueous solutions, 0.3 M oxalic ($H_2C_2O_4$), 0.6 M sulfuric (H_2SO_4), and 1.2 M sulfuric acids, that were used as electrolytes. The detailed conditions for the anodization of the Al/TiN bilayered films are summarized in Table 7-1. The anodization process can be divided into two oxidation stages, i.e., anodic oxidations of the upper aluminum layer and the underlying TiN layer, which can be depicted by the current-time anodization curve. Figure 7-2 shows the current-time anodization curve for Sample A. During the first stage, the upper aluminum layer was anodized to nanoporous AAO containing a scalloped hemispherical oxide barrier under each pore bottom, and the anodic current density was rather steady at about 8 mA/cm^2 except at the initial 2 min. As the downward grown pore channels reached the Al/TiN interface, the anodic current density dropped abruptly to a value less than 0.1 mA/cm^2, and the underlying TiN was oxidized by anodization as well. The anodic oxidation of TiN layer was confined in the AAO pore area and, consequently, led to the formation of nanodot structures with a pattern in accordance with the upper nanoporous AAO layer. The anodic reaction was terminated while the exposed TiN region was fully oxidized to TiO_2.

Figure 7-3(a) shows a cross-sectional transmission electron microscopy (TEM) (JEOL JEM-2010F) image of the bottom of AAO nanopore channels after the

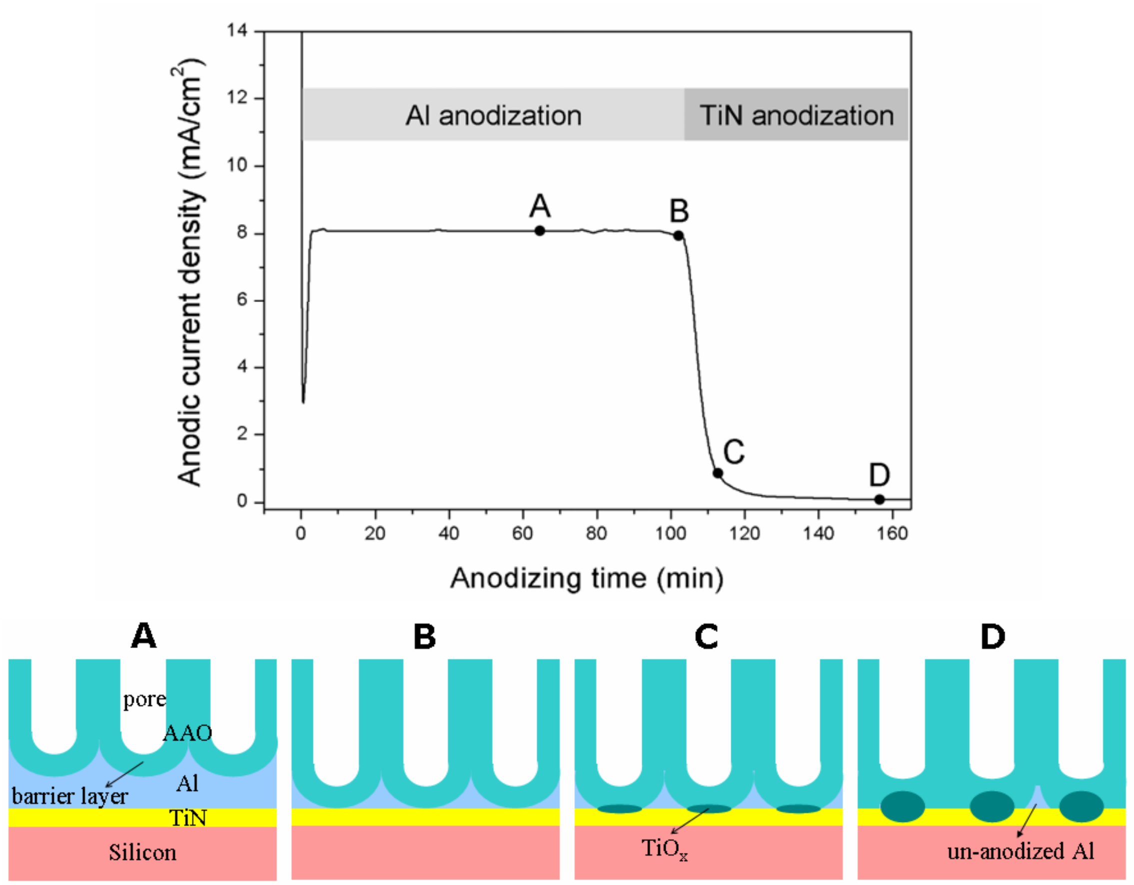

Figure 7-2 Anodic current density-anodizing time behaviors during anodizing of the Al/TiN bilayered films in 0.3 M oxalic acid electrolyte (Sample A). The insets are schematic diagrams showing the anodization steps.

completion of the anodization (Sample A). Figure 7-3(b) presents a diagrammatic illustration of the TEM image. The TEM image clearly shows that there is an isolated dome structure embedded at the interface between the AAO and TiN layer. In order to identify the chemical composition of the dome structure, electron energy loss spectroscopy (EELS) analysis was performed in a TEM system equipped with a cold field emission gun and a Gatan GIF 2000 spectrometer. The detected electrons have undergone core losses within the energy range between 310 and 617 eV, within which the characteristic edges of titanium ($L_{2,3}$-edge), nitrogen (K-edge), and oxygen (K-edge) were measured. Figure 7-4 shows the EELS spectra taken at three different positions of the dome structure as indicated in the inset. Spectrum A was taken at the dome center, which indicates that the dome structure basically consists of titanium and oxygen. However, the fine structure of the oxygen K-edge peak is not comparable to TiO_2 from literatures[Moltaji 2000-381], suggesting that the dome is likely composed of non-stoichiometric TiO_x. Spectrum B was taken at the dome bottom, and reveals that there is

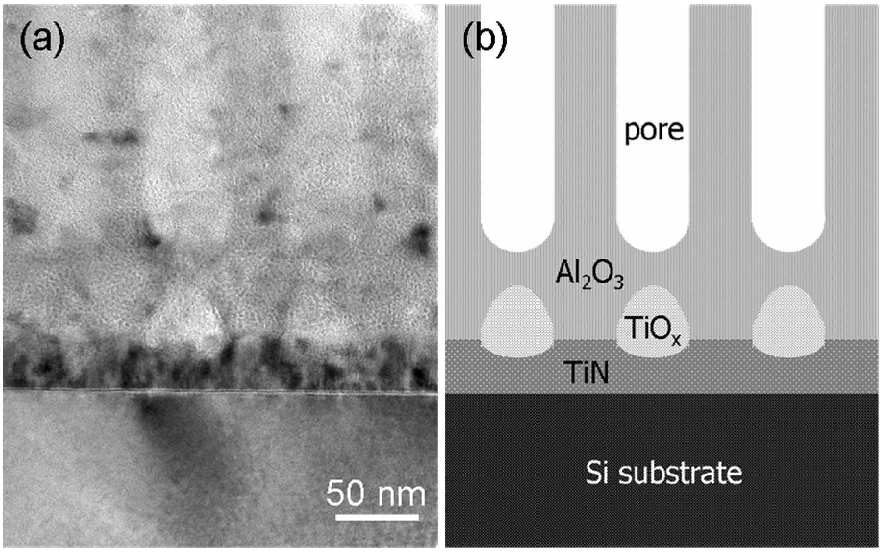

Figure 7-3 (a) Cross-sectional TEM image of the bottom of AAO nanopore channels after the completion of the anodization (Sample A). (b) Diagrammatic illustration of the TEM image in (a).

a TiO_xN_y transition layer formed between the underlying TiN layer and the top TiO_x dome. With regard to the underlying TiN layer, little oxygen *K*-edge peak is detected in the EELS spectrum (spectrum C), indicating that anodization of the underlying TiN layer was not complete. The EELS study clearly shows that the dome structure was derived from anodization reaction of the underlying TiN layer. While the anodization process proceeds, an oxygen concentration gradient develops, which correlates closely with the diffusion rate of oxygen-containing ions (O^{2-} and/or OH^-) from the

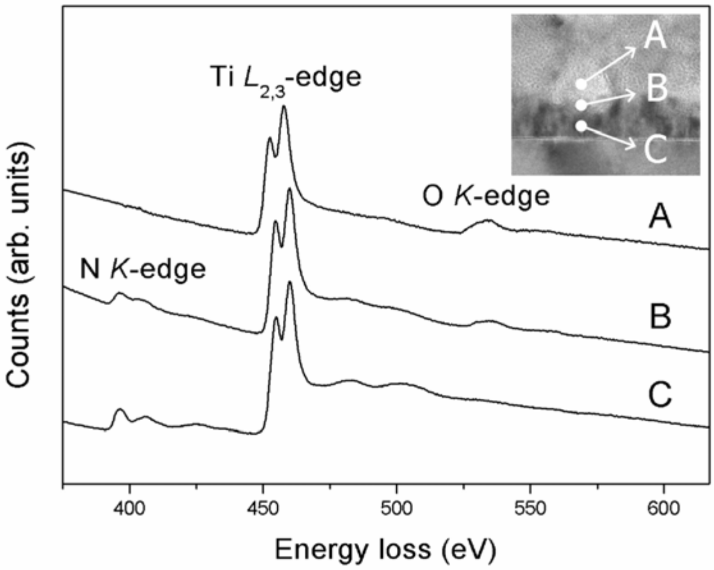

Figure 7-4 EELS spectra showing the titanium $L_{2,3}$-edge, nitrogen *K*-edge, and oxygen *K*-edge. The spectra correspond to three different positions as shown in the inset: (A) At the center, (B) at the bottom, and (C) at the underside of the titanium oxide dome (Sample A).

electrolyte. Thus, anodization of TiN is most efficient in the upper portion of the underlying TiN layer. The TiO_x bulge resulting from oxidation of the TiN layer is accompanied by a volume expansion. For example, the molar volume increase is about 60% as TiN is oxidized to TiO_2[Gwo 1999-1090].

The anodization behavior of the Al/TiN film stack on the silicon wafer is regarded to involve two stages and is different from the case of the aluminum film directly deposited on semiconductor substrates. In the earlier stage, the upper aluminum layer is anodized to alumina (Al_2O_3), accompanied by simultaneous outward migration of Al^{3+} and inward diffusion of O^{2-}/OH^- ions driven by the applied electric field, leading to the vertical pore channel growth[Jessensky 1998-1173]. The Al_2O_3 dissolution at the Al_2O_3/electrolyte interface is equilibrium with the Al_2O_3 growth at the Al/Al_2O_3 interface. As the oxide barrier layer at the pore bottom approaches the area adjacent to the Al/TiN interface, anodization of the underlying TiN can be initiated by the following anodic reaction:

$$\mathrm{TiN} + x\,\mathrm{OH}^- \rightarrow \mathrm{TiO_x} + (1/2)\,\mathrm{N_2} + x\,\mathrm{H}^+ \qquad (7.1)$$

The anodic reaction results in the formation of the TiO_x bulges. Finally, the anodic current drops abruptly (less than 0.1 mA/cm^2) and the electrochemical reactions terminate due to the complete conversion of remaining aluminum to Al_2O_3. At the end of the anodic oxidation, the Al_2O_3 barrier layer at pore bottom mantles the TiO_x dome as shown in Figure 7-3(a).

Figure 7-5 shows the selected X-ray photoelectron spectroscopy (XPS) titanium 2*p* peaks as a function of sputter time for the nanodot arrays of titanium oxides (Sample A) after the overlying AAO template was removed by wet chemical etching at 60 °C with a mixed solution of 6 vol.% phosphoric acid (H_3PO_4) and 1.5 wt.% chromic acid (CrO_3). XPS analyses were performed on a ULVAC-PHI 1600 ESCA system with Al-*Kα* (1486.6 eV) excitation. Argon ion with ion energy of 5 keV was used for sputter profiling. As shown in Figure 7-5, for the unsputtered nanodot surface, the measured spectrum of titanium 2*p* only consist of a doublet peak corresponding to the TiO_2 state (Ti-O bond) with peak binding energy for Ti^{4+} $2p_{3/2}$ electrons of 459.0 eV. At the commencement of sputtering, the intensity of the titanium 2*p* doublet decreases gradually, and after 60 sec a shoulder appears at the low energy edge, which then develops into an additional doublet peak in the spectra. The intensity of this second doublet gradually increases and the position of the peak gradually shifts to the lower

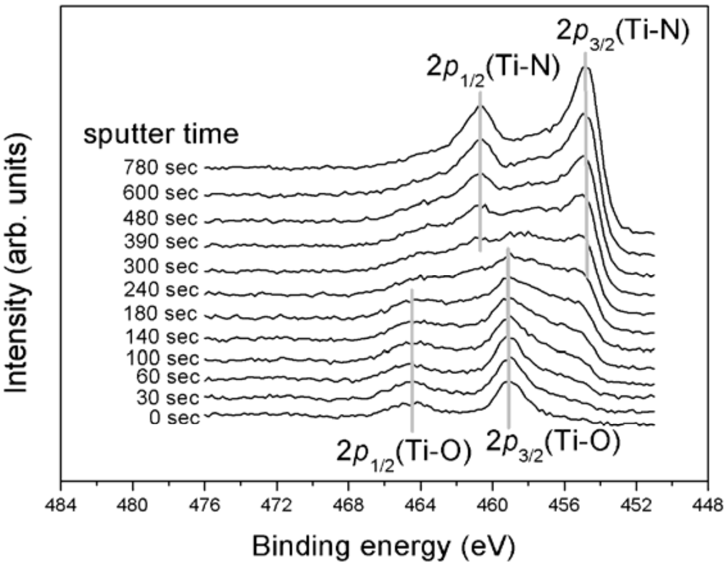

Figure 7-5 XPS titanium 2*p* spectra as a function of sputter time for the nanodot arrays of titanium oxides (Sample A) after the overlying AAO template was removed by wet chemical etching.

energies, making it typical for the TiN state (Ti-N bond) with peak binding energy for Ti^{3+} $2p_{3/2}$ electrons of 455.2 eV. These results imply the transition from stoichiometric TiO_2 at the surface to TiN with the coexistence of both the sub-oxides and oxy-nitrides during the argon ion sputtering. Accordingly, the nanostructured oxide domes formed on TiN by anodic oxidation through the overlying porous AAO template are mainly composed of titanium dioxides, titanium sub-oxides (TiO_x), and titanium oxy-nitrides (TiO_xN_y). The degree of TiN oxidation increases towards the dome surface.

After removing the overlying AAO template, the side- or top-view field-emission scanning electron microscopy (FE-SEM) (Hitachi S-4000) images of the nanodot arrays of titanium oxides anodized under voltages of 40, 20, and 8 V are shown in Figures 7-6(a)-(c), respectively. It is clear from the presented micrographs that the hexagonal arrangement and nearly circular shape of the nanodots are in accordance with the nanopores of the AAO template shown in Figure 4-7, suggesting that the local anodization of TiN takes place only inside the nanopores. However, the ordered hexagonal arrangement of the nanodot is disrupted by domain boundaries (short-range ordering). The ordered domain size is a linear function of the anodizing time correlating closely with the thickness of initial aluminum layer. The size of the locally anodized nanodots can be varied over a wide range because the diameter of the self-ordered AAO nanopores is dependent upon anodization parameters. It turned out that the average diameter of the nanodots prepared from 0.3 M oxalic acid at 40 V (Sample A), 0.6 M sulfuric aid at 20 V (Sample B), and 1.2 M sulfuric acid at 8 V (Sample C) are approximately 66, 30, and 16 nm, respectively. The diameter of the nanodots alters as a

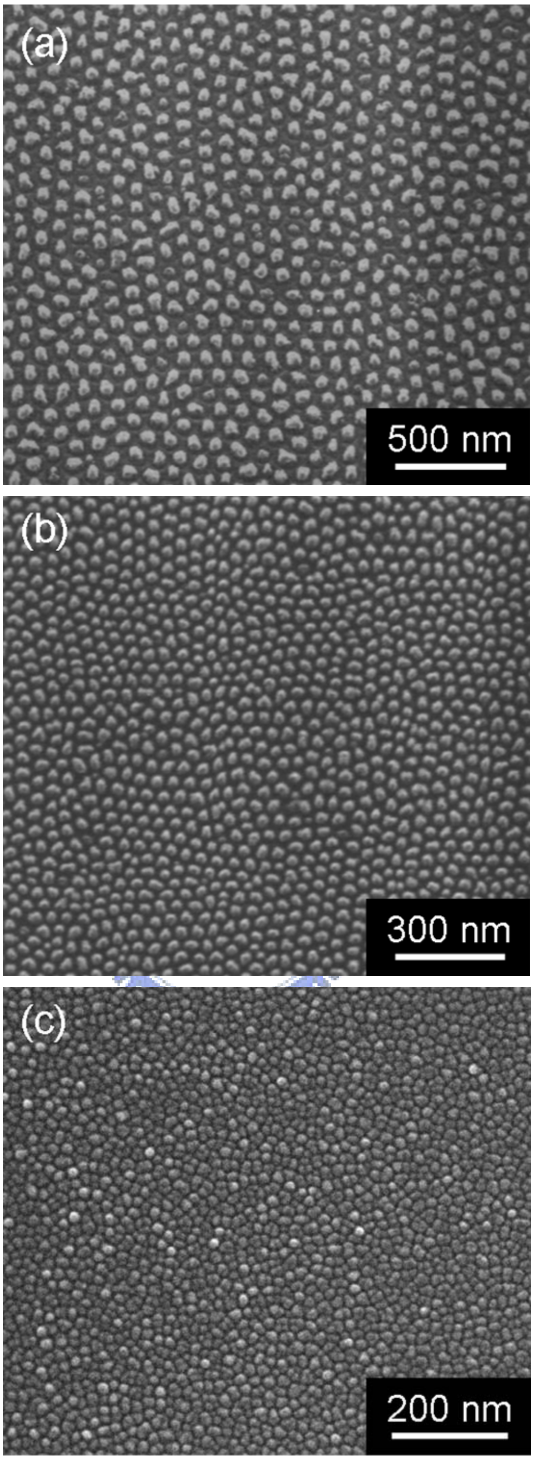

Figure 7-6 Side- or top-view FE-SEM images of nanodot arrays of titanium oxides after the overlying AAO template was removed by wet chemical etching. Anodization was conducted in (a) 0.3 M oxalic acid at 40 V (Sample A), (b) 0.6 M sulfuric acid at 20 V (Sample B), and (c) 1.2 M sulfuric acid at 8 V (Sample C).

function of the anodization voltage. In Figure 7-7, the average dot diameter and interdot

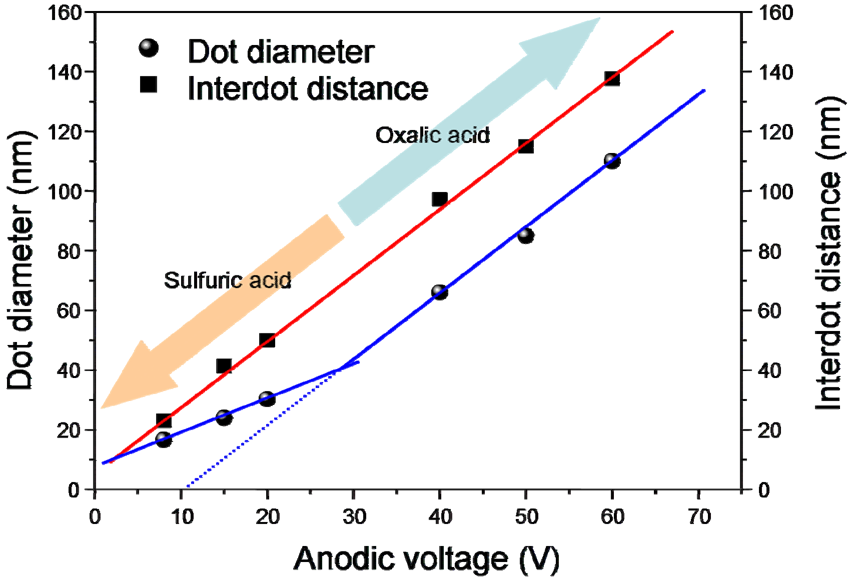

Figure 7-7 Average dot diameter and interdot distance of the obtained titanium oxide nanodots as a function of anodic voltage.

distance of the obtained titanium oxide nanodots are plotted as a function of the anodic voltage. It can be seen that the interdot distance increases linearly with the anodic voltage and is identical with the interpore distance of the AAO nanopores shown in Figure 4-8. As for the dot diameter, it increases with increasing the anodic voltage as well, but the plot shows two linear divisions with different slopes. In the high-voltage region above 40 V (oxalic acid electrolyte), the slope of the fitted line is almost equal to the slope of the fitted line of interdot distance. However, in the region below 20 V (sulfuric acid electrolyte), the slope of the fitted line is remarkably decreased. This suggests that a significantly different oxidation kinetics exists for the sulfuric acid case in the low-voltage regime. During the TiN oxidation, the strong electric field (*E*) resulted from the applied voltage (*V*) enhances the outward diffusion of metallic cations from the substrate and/or the inward diffusion of oxygen-containing anions (O^{2-}/OH^{-}) from the electrolyte across the Al_2O_3 barrier layer under AAO pore bottom. The thickness of the Al_2O_3 barrier layer (D_a) crucially influences the electric field according to the formula $E = V/D_a$ and thus the ion diffusion rates. On the other hand, when a sulfuric acid electrolyte was used, the Al_2O_3 barrier layer was rapidly dissolved and thinned in such a low *p*H solution. As a consequence, the magnified electric field significantly promoted the ion diffusion, leading to the overgrown of the nanodots and thus an observed deviation from the fitted line of dot diameter in Figure 7-7. Moreover, from the figure, one can expect that the isolated feature of the oxide nanodots will disappear and form a continuous oxide film, as the anodic voltage is small than the intersection point of the fitted lines of dot diameter and interdot distance. The smallest diameter of the nanodots produced by this novel approach is supposed to be about 10 nm.

7.3 Shape improvement of TiO_2 nanodots

The nanoporous AAO film can be used as the mask for local anodization of the underlying TiN layer, thereby forming the nanodot arrays of titanium oxides with similar pattern as the upper AAO nanopore arrays. However, the nanodots are irregular in shape because the rough interface between the aluminum and TiN layers of the Al/TiN film stack results in a non-uniform anodic oxidation rate in the TiN layer. In this study, we report on the realization of highly ordered TiO_2 nanodots with uniform shape

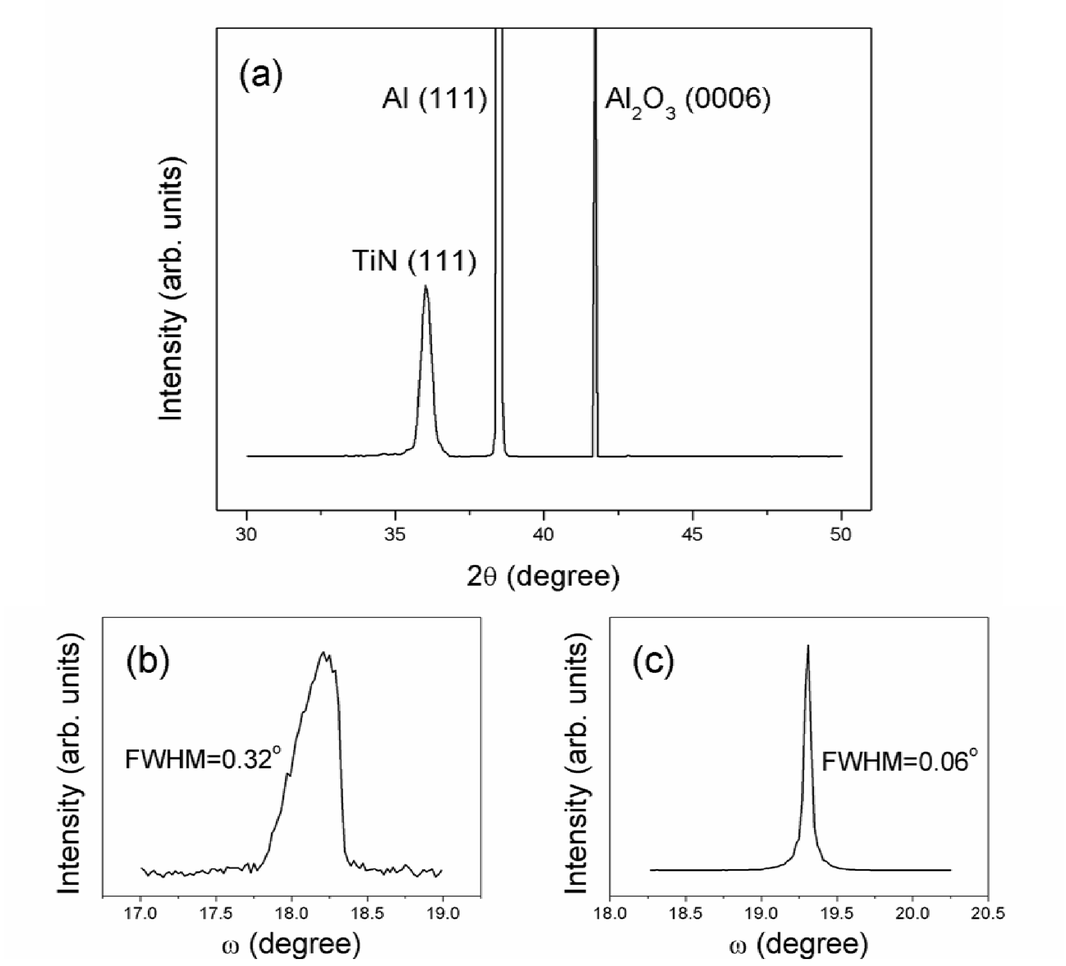

Figure 7-8 (a) XRD *θ*-2*θ* scan of an epitaxial Al/TiN bilayer grown on sapphire (0001). *ω*-rocking curves

from the (b) TiN and (c) Al layers.

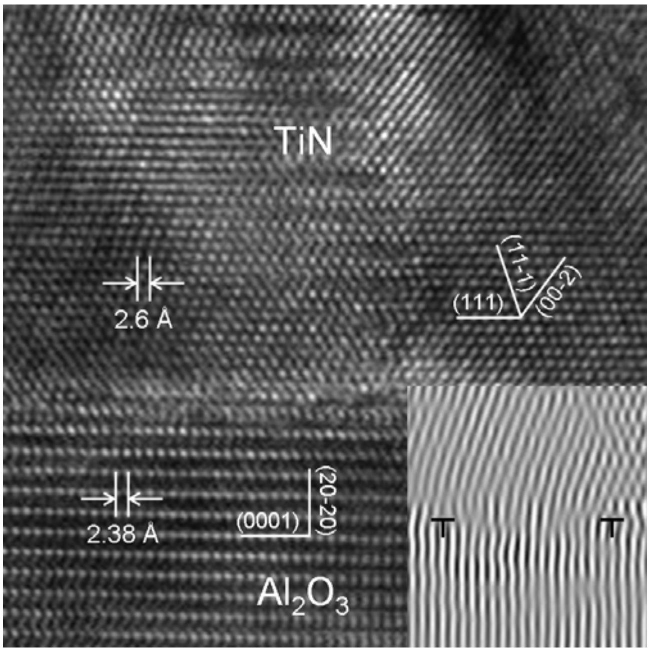

Figure 7-9 Cross-sectional HRTEM image of the epitaxial TiN/sapphire interface. The inset is the corresponding Fourier-filtered lattice image.

on a sapphire substrate by anodization of an epitaxial Al/TiN film stack.

Fabrication of the highly uniform TiO_2 nanodot arrays began with the epitaxial growth of a 10-nm-thick TiN film on (0001)-oriented, 2-inch-diameter sapphire wafers using a reactive dc magnetron sputtering system with a base pressure of 5×10^{-7} Torr. The TiN layer was deposited by dc magnetron sputtering at 300 °C using a titanium target in a mixed nitrogen and argon atmosphere (N_2:Ar = 3:50) under a working pressure of 1×10^{-3} Torr. Following the TiN deposition, an aluminum film about 5 μm in thickness was deposited by thermal evaporation in a high vacuum chamber (< 5×10^{-7} Torr) at 300 °C. The crystallinity and orientation of the as-deposited films were investigated by X-ray diffraction (XRD) (Philips X'Pert Pro). XRD θ-2θ scan and rocking curves were obtained using Cu-$K\alpha$ radiation ($\lambda = 0.1541$ nm). Figure 7-8(a) shows the XRD θ-2θ scan spectrum of the Al/TiN/sapphire heterostructure. In addition to the sapphire (0006) peak, only TiN (111) and Al (111) peaks are presence in the XRD spectrum. The preferential growth of the (111) TiN and (111) Al films suggests the highly oriented growth in sequence of the film stack on the (0001) sapphire. The full-width at half maximum (FWHM) for TiN (111) and Al (111) obtained from the rocking curves shown in Figures 7-8(b) and (c) are 0.32 and 0.06, respectively, the rather low FWHM values adequately implying epitaxial growth of the films. Although the lattice mismatch between the (111) plane of the TiN film and the (0001) plane of

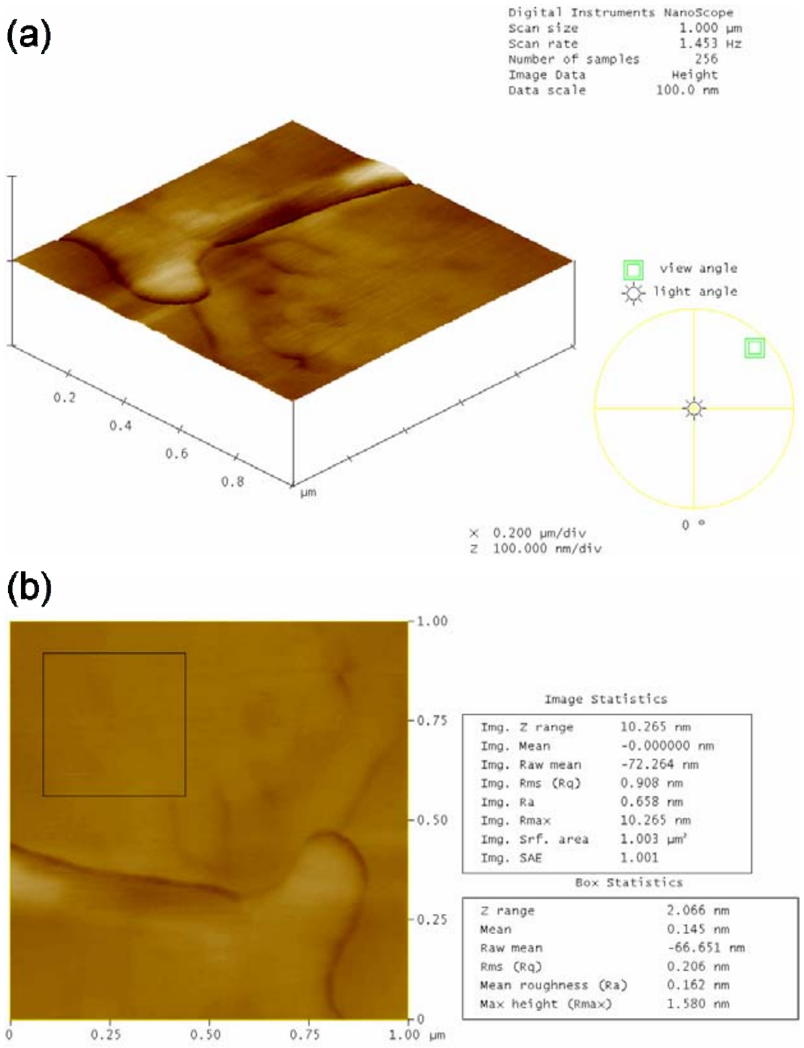

```
Digital Instruments NanoScope
Scan size             1.000 µm
Scan rate             1.453 Hz
Number of samples       256
Image Data            Height
Data scale          100.0 nm
```

```
              Image Statistics
Img. Z range        10.265 nm
Img. Mean           -0.000000 nm
Img. Raw mean       -72.264 nm
Img. Rms (Rq)       0.908 nm
Img. Ra             0.658 nm
Img. Rmax           10.265 nm
Img. Srf. area      1.003 µm²
Img. SAE            1.001
                 Box Statistics
Z range                      2.066 nm
Mean                         0.145 nm
Raw mean                     -66.651 nm
Rms (Rq)                     0.206 nm
Mean roughness (Ra)          0.162 nm
Max height (Rmax)            1.580 nm
```

Figure 7-10 Contact-mode AFM images (1×1 μm^2) of the epitaxial aluminum surface: (a) 3D diagram; (b) roughness analysis.

sapphire is as high as 8.46%, misfit dislocations arranged almost periodically on the interface can relieve the lattice mismatch[Chen 2003-208]. Figure 7-9 shows the cross-sectional high-resolution TEM (HRTEM) image of the epitaxial TiN/sapphire interface and the corresponding Fourier-filtered lattice image. The images indicate that there are extra crystal planes on the sapphire substrate side. In fact, eleven times of 0.26 nm is almost equal to twelve times of 0.238 nm. Therefore, the large mismatch is relieved by an array of the misfit dislocations on the interface.

For preparation of TiO_2 nanodot arrays, the epitaxial Al/TiN bilayered films were directly oxidized by electrochemical anodization without any pre-planarization step. Figure 7-10 shows the atomic force microscopy (AFM) (Digital Instruments NanoScope Ⅱ) images of the epitaxial aluminum surface before the anodization. An atomically-flat aluminum surface (mean roughness, Ra ~ 1.6 Å) with terraces and steps was observed.

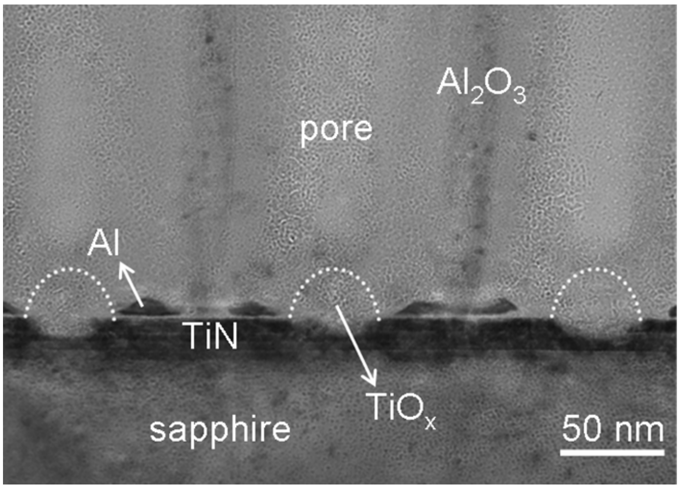

Figure 7-11 Cross-sectional TEM image of the bottom of AAO nanopore channels after the completion of the anodization of epitaxial Al/TiN bilayered films. The dashed lines indicate the interface between TiO$_x$ nanodot and upper Al$_2$O$_3$ barrier layer.

Anodization was carried out in a 0.3 M oxalic acid solution at 21 °C under a constant polarization voltage of 40 V. Figure 7-11 shows a cross-sectional TEM image of the bottom of AAO nanopores after the completion of the anodization. The anodic oxidation of the TiN layer was confined in the AAO pore area and thereby isolated dome structures of titanium oxides were formed at the interface between the AAO and TiN layers. At the end of the anodization, the TiO$_x$ dome is surrounded by un-anodized aluminum metal and mantled by Al$_2$O$_3$ barrier. Chemical phases labeled in Figure 7-11 were characterized by EELS and energy dispersive spectroscopy (EDS).

Figure 7-12(a) shows the top-view FE-SEM image of the nanodot arrays of titanium oxides after removing the nanoporous AAO. The self-organized nanodots have a uniform size distribution with a diameter of about 66 nm and an interdot distance of about 100 nm. The nanodots are grouped into domains, and within a dot array domain, ordered nanodots with a hexagonal arrangement can be clearly observed. Most nanodots duplicate the circular shape of the AAO nanopores except those at domain boundaries. The morphology of the TiO$_x$ nanodots should be strongly affected by the diffusion path of oxygen-containing ions (O^{2-} and/or OH^- from electrolyte) near the Al/TiN interface of the Al/TiN film stack because the oxidation rate of the TiN layer is mainly determined by the concentration of O^{2-}/OH^- ions nearby[Jessensky 1998-1173]. A rough interface between the aluminum and TiN layers leads to a non-uniform diffusion rate of O^{2-}/OH^- ions at the interface and thus results in irregular ion concentration distribution around the growing nanodots. As can be seen in Figure 7-12(c), nanodots prepared from a polycrystalline Al/TiN film stack had an irregular dome shape with a coarse base structure, which is primarily a reflection of the rough interface between the aluminum and TiN layers. In addition, the polycrystalline Al/TiN interface has a higher defect density (such as grain boundary, dislocation, vacancy, etc.) leading to a non-uniform ion transport through the interface. In grain boundaries, the diffusion coefficient of oxygen species is several orders of magnitude greater than that of volume diffusion coefficient [Farver 1998-189]. Migration of O^{2-}/OH^{-} ions is more rapid along grain boundaries, dislocations, and external surfaces than in the interior of crystals, resulting in the formation of TiO_x nanodots with a rough dome structure could not faithfully duplicate the circular shape of the AAO nanopores. In contrast, the epitaxial Al/TiN film stack has a smoother interface and lower defect density, and, therefore, can produce circular nanodots with a smoother surface [see Figure 7-12(b)].

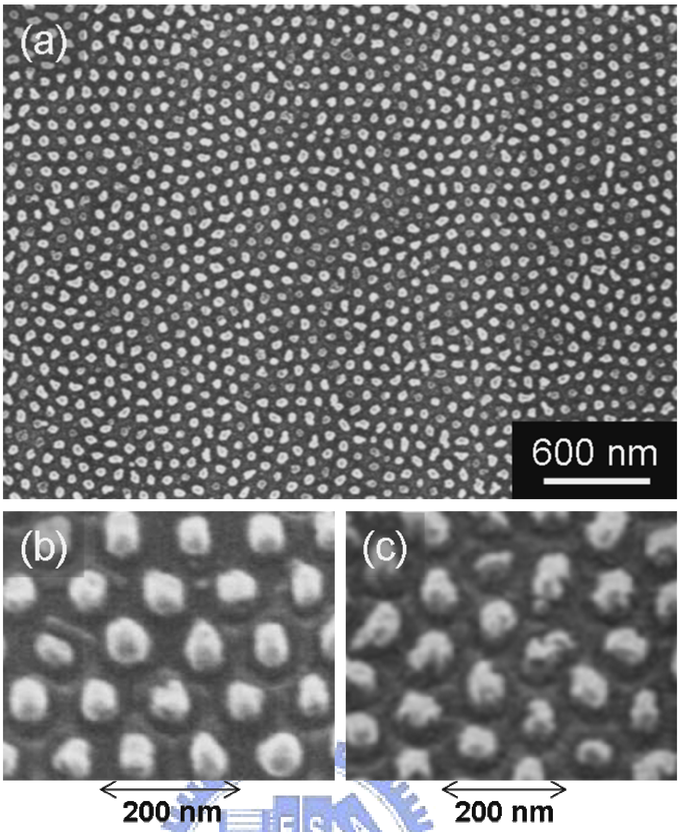

Figure 7-12 (a) Top-view and (b) side-view FE-SEM images of the nanodot arrays of titanium oxides prepared from the epitaxial Al/TiN film stack. (c) Side-view image of the nanodots prepared from the polycrystalline film stack.

7.4 Phase stability of TiO_2 nanocrystals

Phase transformation of TiO_2 has been widely studied owing to both scientific interest and technological applications. TiO_2 has three crystalline phases, i.e., rutile, anatase, and brookite. Rutile is the thermodynamically stable phase in all temperatures and pressures, while anatase and brookite are metastable phases[Kumar 1995-873]. Anatase is the TiO_2 phase of the greatest commercial interest, although it is seldom found in natural ore. However, when the crystal size decreases below a certain size, anatase phase becomes more stable than rutile[Zhang 2000-3481]. This kind of size effect on the relative stability of nanophases also occurs in graphite[Zhao 2002-234], alumina[McHale 1997-788], ZnS[Zhang 2003-13051], and CdSe[Jacobs 2001-1803]. It is well known that as the size of a particle decreases, surface/volume ratio increases. Therefore, surface free energy (γ) and surface stress (f) will have contribution on phase stabilities of different phases. According to available data of γ, f, and corresponding Gibbs free energy (G) of the bulk phases, the equilibrium size of different phases can be calculated.

For the phase transformation of nanocrystalline anatase to rutile, the change of the molar standard free energy (ΔG^{o}) (J/mol) can be described as[Zhang 1998-2073]

$$\Delta G^{\mathrm{o}} = \Delta_{\mathrm{f}} G_{\mathrm{r}}^{\mathrm{o}} - \Delta_{\mathrm{f}} G_{\mathrm{a}}^{\mathrm{o}} + (2\varepsilon + 3)\frac{2M}{D}\left(\frac{\gamma_{\mathrm{r}}}{\rho_{\mathrm{r}}} - \frac{\gamma_{\mathrm{a}}}{\rho_{\mathrm{a}}}\right) \tag{7.2}$$

where $\Delta_{\mathrm{f}}G^{\mathrm{o}}$ is the standard free energy of formation; ε is the ratio of surface stress to surface free energy (assumed to be about 1); M is the molecular weight of TiO_2 (79.87 g/mol); D is the average diameter of nanoparticles; ρ is the density of TiO_2 (4.25 and 3.89×10^6 g/m^3 for rutile and anatase, respectively); and the subscripts r and a represent rutile and anatase, respectively.

In the temperature (T) range from 298 to 1000 K, data for the standard free energy of formation of rutile and anatase taken from the JANAF thermochemical tables[Chase 1985] are, respectively,

$$\begin{aligned}\Delta_{\mathrm{f}} G_{\mathrm{r}}^{\mathrm{o}} &= -9.539962\times10^5 + 3.040222\times10^2 T - 1.683551\times10 T\ln T + \\ &3.166423\times10^{-3} T^2 + 6.748623\times10^5 T^{-1}\end{aligned} \tag{7.3}$$

$$\begin{aligned}\Delta_{\mathrm{f}} G_{\mathrm{a}}^{\mathrm{o}} &= -9.491471\times10^5 + 3.211113\times10^2 T - 1.927547\times10 T\ln T + \\ &4.039531\times10^{-3} T^2 + 7.533409\times10^5 T^{-1}\end{aligned} \tag{7.4}$$

According to Zhang and Banfield[Zhang 1998-2073], the surface free energy (J/m^2) for rutile and anatase are, respectively,

$$\gamma_{\mathrm{r}} = 1.91 - 1.48\times10^{-4}(T - 298) \tag{7.5}$$

$$\gamma_{\mathrm{a}} = 1.32 - 1.48\times10^{-4}(T - 298) \tag{7.6}$$

Inserting the standard free energies of formation [Equation (7.3) and (7.4)] and

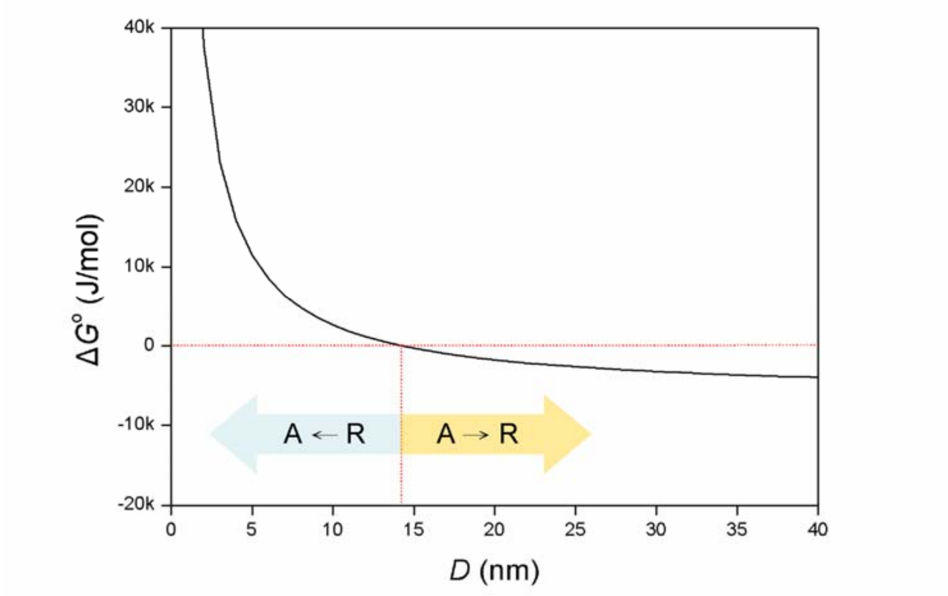

Figure 7-13 The variation of the free energy difference between nanocrystalline rutile and anatase with particle diameter at 300 K.

the surface free energies [Equation (7.5) and (7.6)] into Equation (7.2), and letting T = 300 K, we obtain

$$\Delta G^{o}(\mathrm{J/mol}) = -6140.9047 + \frac{87921.0120}{D} \qquad (7.7)$$

where D is in nm. Figure 7-13 shows the variation of ΔG^{o} with D at 300 K. The particle sizes crucially determine the thermodynamic phase stability at ultrafine sizes. According to the calculated results, when particle size decreases below *ca*. 14 nm, the total free energy of rutile is higher than that of anatase, the relative phase stability of anatase and rutile reverses, and anatase becomes the thermodynamically stable phase. This is a consequence of the fact that rutile has a higher surface energy than anatase, and thus the relative phase stability of anatase and rutile reverses as the particle size is reduced to a critical value.

7.5 Phase development of TiO_2 nanodots

In this study, the as-prepared nanodots of titanium oxides are basically amorphous, but they can later be converted to crystalline TiO_2 by annealing. Prior to annealing, un-anodized aluminum and TiN surrounding the nanodots, as shown in Figure 7-11, were removed by reactive ion etching (RIE) using a gas mixture of Cl_2 and BCl_3. The flow rate of Cl_2 and BCl_3 was all 20 sccm. The working pressure of the RIE system was

1×10^{-2} Torr with an inductively coupled plasma (ICP) power of 750 W and a rf bias

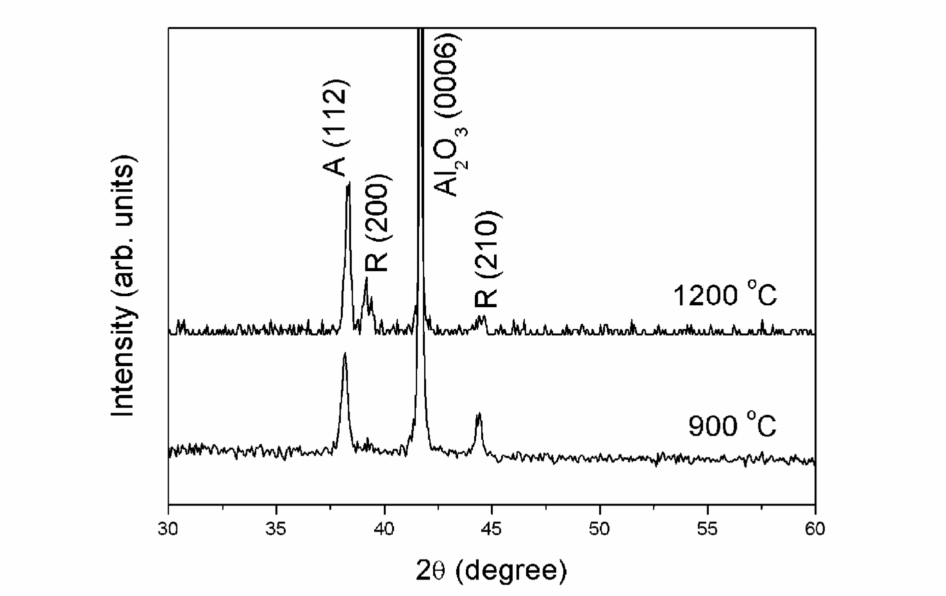

Figure 7-14 XRD θ-2θ scan of the TiO_2 nanodot arrays after annealing in oxygen atmosphere for 1 hour. The diffraction peaks for anatase phase and rutile phase are marked with A and R, respectively.

power of 120 W. Annealing was performed at temperature higher than 900 °C in a furnace with a flowing oxygen atmosphere for 1 hour. The XRD θ-2θ scan spectra of the TiO_2 nanodot arrays after annealing are shown in Figure 7-14. After annealing at 900 °C, obvious diffraction peaks of anatase (112) and rutile (210) are observed, indicating that polycrystalline TiO_2 nanodots are formed. Figure 7-15 shows the cross-sectional HRTEM image of the TiO_2 nanodot/sapphire interface. From the HRTEM image, the polycrystalline nanodot consists of two dominant grains of anatase and rutile (grain boundary is marked by white arrows) accompanied by several smaller grains. Two enlarged images of the anatase grain and rutile grain are given in the insets. The lattice fringes with a spacing of 4.76 Å in the left inset and 3.24 Å in the right inset corresponds to the spacing between the (002) planes of anatase and the (110) planes of rutile, respectively. When the nanodots are annealed at a higher temperature of 1200 °C, the XRD spectrum in Figure 7-14 clearly shows that the anatase phase still exists and predominates over the rutile phase in the nanodots. Moreover, rutile gradually transferred the orientation from (210) to (200), which may result from a better lattice match between the rutile (200) and sapphire (0001) planes[Schuisky 2000-3319]. According to Figure 7-16, the lattice mismatch values between the (200) plane of rutile and the (0001) plane of sapphire were calculated to be -3.49% along the [010] rutile direction and 7.21% along the [001] rutile direction.

The anatase-to-rutile phase transformation of TiO_2 is believed to be spontaneous,

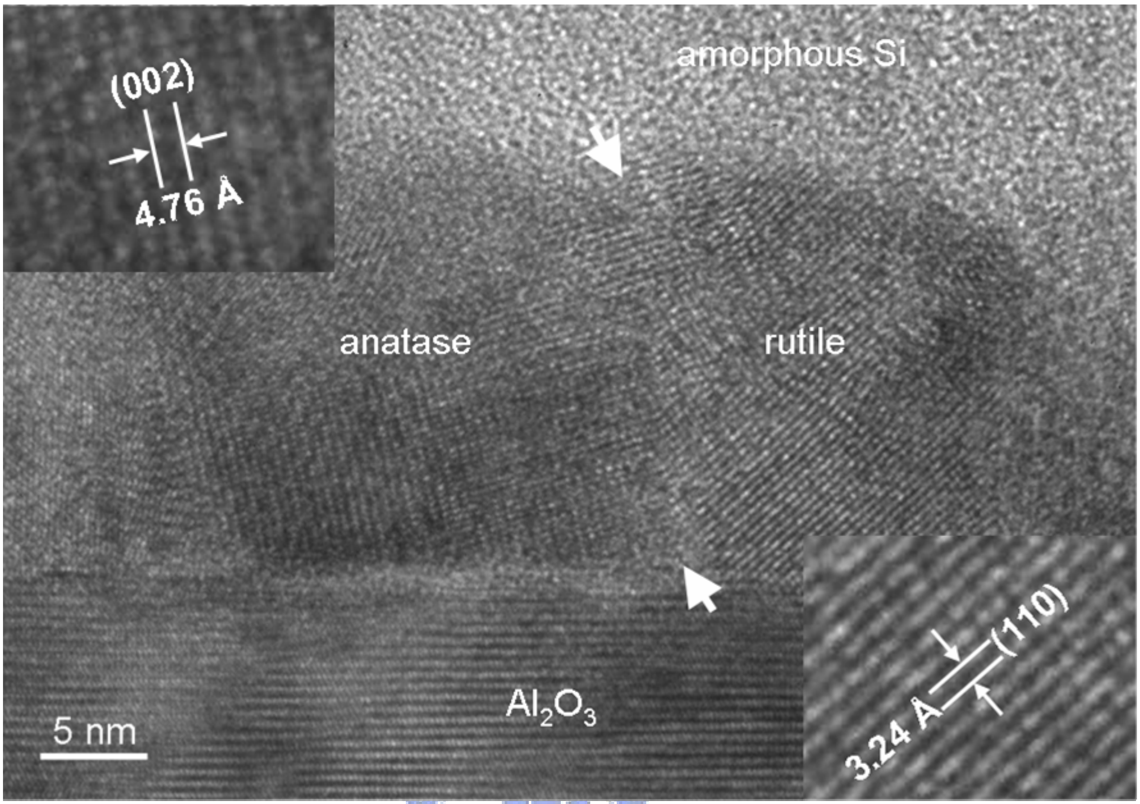

Figure 7-15 Cross-sectional HRTEM image of the TiO_2 nanodot/sapphire interface after annealing at 900 °C. The sample was covered with an amorphous silicon film to protect the nanodots. The grain boundary is indicated by two white arrows. The left and right insets are the enlarged images of the anatase grain and rutile grain, respectively.

and is kinetically favorable at high temperatures[Kumar 1995-873]. However, it is interesting to note that the TiO_2 nanodots formed in the study can maintain a stable anatase phase at temperatures as high as 1200 °C. This is quite different from the cases of TiO_2 thin films and powders. During the crystallization process of TiO_2 nanodots, anatase grains first nucleate and then grow to a critical size, which will in turn provide nucleation sites for the development of the rutile phase[Gouma 1999-1231]. When the anatase grain reaches a critical size, the transformation of anatase to rutile begins and proceeds very rapidly[Wang 1999-3113]. The driving force for the phase transformation is the difference in free energies between the anatase and rutile phases. The rutile grain will keep growing at the expense of the surrounding anatase phase until the remaining anatase phase diminishes to a critical size. According to thermodynamic analyses, the stability of the anatase phase depends largely on the grain (particle) size[Zhang 1998-2073]. As shown in Figure 7-13, when the particle size decreases below *ca.* 14 nm, the total free energy of rutile is higher than that of anatase. Because rutile has a higher surface energy than anatase, the relative phase stability of anatase and rutile will reverse as the particle size is reduced to a critical value. Since the TiO_2 nanodot is isolated, an increase in the volume of the rutile phase will lead to a decrease in the anatase content. As the size of the anatase grains is diminished to the critical size, the phase transformation is terminated, resulting in a stable coexistence of the two phases in the nanodots. Therefore, the anatase phase can exist in the TiO_2 nanodots even at a considerably high temperature. However, the sizes of anatase and rutile grains shown in Figure 7-15 are slightly bigger than the critical size (*ca.* 14 nm) determined from the thermodynamic calculations. This is the consequence of that the actual grains are polygonal rather than spherical leading to the deviations from the calculation results. From the above discussion, we expect that the TiO_2 nanodots with a pure anatase phase may be accomplished when the size of the nanodots is smaller than the critical size for the rutile formation.

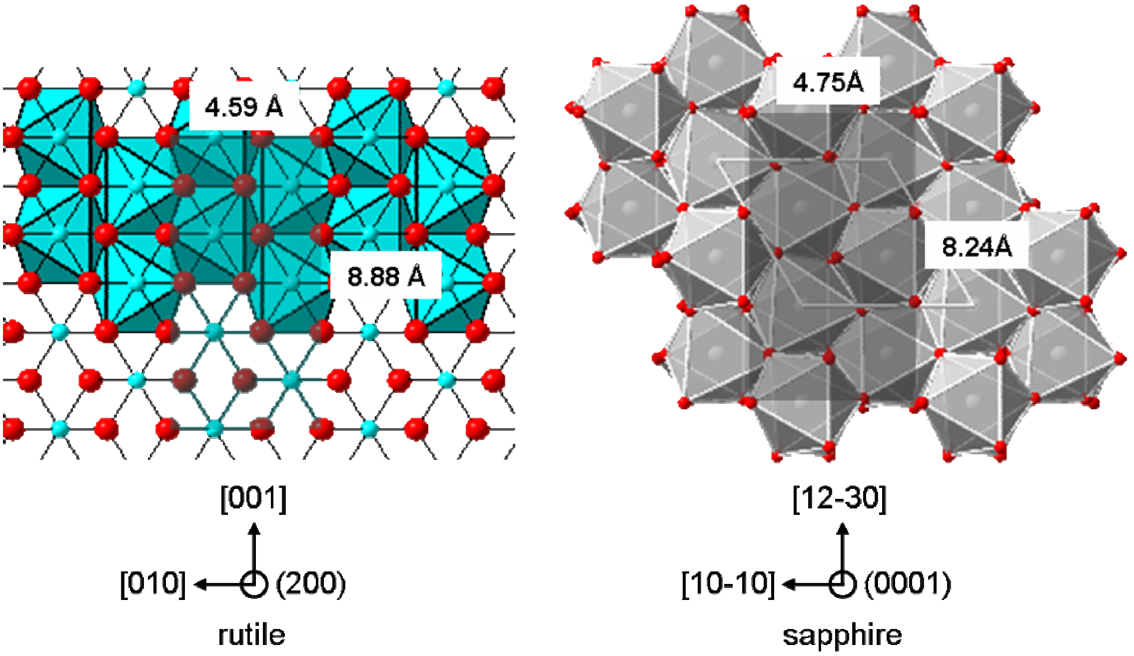

Figure 7-16 Schematic atomic arrangements of the rutile (200) and the sapphire (0001) surfaces.

7.6 Summary

Ordered nanodot arrays of titanium oxides were prepared from Al/TiN bilayered films on silicon wafers by electrochemical anodization. The hexagonal pore arrays of the AAO templates can faithfully duplicate an ordered pattern for the titanium oxide nanodots. The average size of the nanodots is very close to the diameter of the AAO nanopores, and adjustable depending on anodization conditions. TEM, FE-SEM, EELS, and XPS were utilized to determine the microstructure and chemical composition of the nanodots. The as-prepared nanodots are basically amorphous and composed of stoichiometric TiO_2 surface, non-stoichiometric TiO_x interior, and TiO_xN_y bottom. In order to improve the non-uniform shape of the nanodots, we have fabricated highly ordered nanodot arrays of TiO_2 prepared from an epitaxial Al/TiN film stack on a sapphire substrate. The epitaxial Al/TiN interface with a lower interfacial roughness and defect density provides a uniform diffusion rate of O^{2-}/OH^- ions and, consequently, contributes to the formation of smooth nanodots. After high temperature annealing, the XRD and HRTEM results confirm that the TiO_2 nanodots are polycrystalline in nature and mainly consist of two dominant grains of anatase and rutile phases. Because the high temperature crystallization process is confined in the isolated dome structure, the grain growth and a complete anatase-to-rutile phase transition are retarded, resulting in the coexistence of the anatase and rutile phases in the nanodots. We expect that TiO_2 nanodots with a single phase of anatase can be realized as the size of the nanodots is smaller than the critical nuclei size for rutile formation.